Estimating mountain glacier surface temperatures from Landsat-ETM+ thermal infrared data: A case study of Qiyi glacier, China

Yuwei Wu [a,b], Ninglian Wang [a,c,*], Jianqiao He [a], Xi Jiang [d,e]

[a] State Key Laboratory of Cryospheric Sciences, Cold & Arid Regions Environmental & Engineering Research Institute, Chinese Academy of Sciences, Lanzhou 730000, China
[b] University of Chinese Academy of Sciences, Beijing 100049, China
[c] Chinese Academy of Sciences Center for Excellence in Tibetan Plateau Earth Sciences, Beijing 100049, China
[d] Center for Data Assimilation Research and Application, School of Atmospheric Science, Nanjing University of Information Sciences & Technology (NUIST), Nanjing 210044, China
[e] Key laboratory of meteorological disaster (NUIST), Ministry of education, Nanjing 210044, China

ARTICLE INFO

ABSTRACT

Surface temperatures on mountain glaciers are a direct reflection of the heat budget at the glacier surface, which controls the degree of ablation. An understanding of surface temperatures is therefore crucial in simulating the evolution of mountain glaciers and in understanding a glacier's response to climate change. In situ observations indicate that when the exitance angle equals 75°, relative to the nadir angle, the emissivity variation at $\lambda = 12.5\ \mu m$ in bare ice is as much as 0.24. However, research involving the remote-sensing-retrieval of mountain glacier surface temperatures does not generally take into account the topography (i.e., the exitance angle), and the validation of remote sensing approaches using surficial climate measurements on mountain glaciers is lacking. Here we utilize the ETM+ multispectral dataset and resampled water vapor content data from MOD05, combined with the emissivity model of ice and snow, taking the exitance angle into account (Hori et al., 2013), and employ the single-channel algorithm developed by Jiménez-Muñoz et al. (2009), to calculate the remote-sensing-retrieved surface temperature distribution across Qiyi glacier, China, from July 2012 to September 2013. The remote-sensing-retrieved temperatures are validated by the 10-min mean measurements of surface temperature from two automatic weather stations at different altitudes on the glacier, and the results show good agreement at the two sites, with an average bias of 0.96 K and an average root mean square error of 1.5 K. Of note, in summer the influence of thermal emissions from surrounding topography means that the error associated with retrieved temperatures for the glacier tongue and margins might exceed 1.5 K.

© 2015 Elsevier Inc. All rights reserved.

1. Introduction

Earth surface temperature is a reflection of the exchange of all the energy fluxes at the surface–atmosphere interface, and it directly influences the physical and chemical processes between the surface and atmosphere at all scales, thus forming a critical component in hydrological, meteorological, climatological, and environmental studies (Anderson, Norman, Diak, Kustas, & Mecikalski, 1997; Anderson et al., 2008, 2011; Brunsell & Gillies, 2003; Karnieli et al., 2010; Kerr, Lagouarde, Nerry, & Ottlé, 2004; Kustas & Anderson, 2009; Weng, Lu, & Schubring, 2004; Zhang et al., 2008). There have been numerous remote-sensing-retrieval studies involving sea surface temperature (SST) and land surface temperature (LST), and various algorithms have been developed based on each sensor type (Becker & Li, 1990; Gillespie et al., 1998; Hook, Gabell, Green, & Kealy, 1992; Jiménez-Muñoz & Sobrino, 2003; Jiménez-Muñoz et al., 2009; Kealy & Hook, 1993; Kerr, Lagouarde, & Imbernon, 1992; Kerr et al., 2004; Li & Becker, 1993; Li et al., 2013a, 2013b; Price, 1984; Qin, Karnieli, & Berliner, 2001; Sobrino, Jiménez-Muñoz, & Paolini, 2004; Sobrino & Romaguera, 2004; Tonooka, 2001; Wan & Dozier, 1996; Wan & Li, 1997). However, the complex topography of mountain glaciers (i.e., the rapid variations in exitance angle over a small area) and difficulties in obtaining field measurements in these remote, arduous terrains have limited attempts to develop a precise and efficient way for the remote-sensing-retrieval of LST on mountain glaciers and to validate such data.

LST on mountain glaciers may directly reflect the responses of such glaciers to climate change. Although only 4% of the earth's total land ice area is composed of glacier ice, glacier ice mass loss may have contributed to as much as 30% of 20th century sea-level change, and the rate of mass loss has shown a worrying increasing trend in response to recent global warming (Dyurgerov & Meier, 1997, 2000; Gardner et al., 2013; Jacob, Wahr, Pfeffer, & Swenson, 2012; Meier, 1984; Owen et al., 2009). Additionally, air temperature can provide an estimate of glacier mass loss in either a mountain glacier energy–mass balance model or a glacial hydrological model (Arnold, Willis, Sharp, Richards,

& Lawson, 1996; Gurgiser, Marzeion, Nicholson, Kaser, & Ortner, 2013; Hock, 1999, 2003, 2005; Hock, Jansson, & Braun, 2005; Huss, Farinotti, Bauder, & Funk, 2008; La Frenierre & Mark, 2014; Willis, Arnold, & Brock, 2002; Yong, Shiyin, & Yongjian, 2007; Zhang et al., 2013), as glacier ablation has a strong dependence on glacier surface temperature (GST), which in turn reflects the distribution of heat and determines the amount of ablation on the glacier surface. Therefore, the accurate retrieval of LST on mountain glaciers is of great importance in the future development of energy–mass balance and glacial hydrology models that reflect the evolution of these delicate systems.

The most common types of sensors for LST retrieval are AVHRR, MODIS, TM, ETM +, and ASTER; AVHRR and MODIS have been successfully applied to the assessment of surface temperature variations across ice sheets (Comiso, 2000, 2006; Hall et al., 2012, 2013; Koenig & Hall, 2010; Wang & Key, 2003; Wang, Wang, & Zhao, 2013), but their coarser spatial resolution (≥1 km) limits their applicability on mountain glaciers with much smaller spatial coverage. Among these types of sensors, the ETM + thermal infrared band has the finest spatial resolution (60 m); thus, we employed this sensor to retrieve LST and to determine the reliability of the sensor on mountain glaciers. Three effective algorithms have been proposed to retrieve LST using ETM + data (Barsi, Barker, & Schott, 2003; Jiménez-Muñoz & Sobrino, 2003; Jiménez-Muñoz et al., 2009; Qin et al., 2001; Sobrino et al., 2004): the Radiative Transfer Equation (RTE method) (an atmospheric correction algorithm), the mono-window algorithm developed by Qin et al. (2001) (herein the Qin algorithm), and the single-channel algorithm developed by Jiménez-Muñoz and Sobrino (2003) (herein the JM algorithm). However, the RTE method needs atmospheric constraints at the moment of the satellite pass to accurately retrieve LST, which are difficult to obtain on mountain glaciers. One of the three input variables for the Qin algorithm (i.e., mean air temperature) is also difficult to accurately evaluate because of the complex topography of the glacier surface. The JM algorithm is thus selected to retrieve LST on mountain glaciers, because it requires only two input variables (the emissivity and water content of the atmosphere), both of which can be accurately obtained from satellite-derived observations.

Previous research has indicated that the emissivity of ice and snow is affected by the exitance angle (Hori et al., 2006); in situ observations indicate that when the exitance angle is equal to 75°, relative to the nadir angle, the emissivity change at $\lambda = 12.5$ μm for bare ice is as much as 0.24. Although some LST research has been performed to retrieve LST over large areas, including mountain glaciers, the snow and ice emissivity is generally either prescribed or reanalyzed from laboratory and/or field observations without accounting for the exitance angle (Anul Haq, Jain, & Menon, 2012; Gillespie et al., 1998, 2011; Hall et al., 2008; Hulley, Hook, & Baldridge, 2008; Kealy & Hook, 1993; Matsunaga, 1994; Salisbury, D'Aria, & Wald, 1994; Wan, 2008; Wan, Zhang, Zhang, & Li, 2002). To address this shortcoming, we employed the emissivity model of Hori et al. (2013), which takes the exitance angle into account, using the resampled water vapor content of the MOD05 data, which was obtained ~20 min after the Landsat-ETM + data, as input data for the JM algorithm to retrieve the LST distribution across Qiyi glacier. To validate the accuracy of the retrieval results, the retrieved LST is compared with the 10-min mean surface measurements that span the satellite pass times.

2. Data and methods

2.1. Study area

Qiyi glacier (39°14.22′N, 97°45.34′E), on the northern edge of the Qinghai–Tibetan Plateau (Fig. 1), is the first glacier that was extensively studied by Chinese glaciologists (Snow and Ice Research Team of Chinese Academy of Sciences) in 1958. Classified as a sub-continental glacier, Qiyi glacier is a small cirque–valley glacier that covers an area of 2.698 km² and was 3.66 km long in 2005 (Jiang, Wang, He, Wu, &

Song, 2010; Wang, He, Pu, Jiang, & Jing, 2010). It is strongly influenced by westerlies and the Asian summer monsoon, with both precipitation and ablation primarily occurring during the summer months, which is characteristic of most glaciers and ice caps on the Qinghai–Tibetan Plateau. The Global Digital Elevation Model (GDEM, version 2) obtained from the Advanced Spaceborne Thermal Emission and Reflection Radiometer (ASTER) shows that the glacier extends from 5145 m at its highest elevation to 4310 m at its terminus, with a maximum slope of 51.1°. In July 2011, two autonomous weather stations (AWSs) were installed on Qiyi glacier, at 4410 m and 4470 m altitude, to measure the glacier surface temperature and other climate variables, which can be used to validate the remote-sensing-retrieved GST in the present study. Sensor details for each AWS are provided in Table 1.

We calculated the Normalized Difference Snow Index (NDSI) using ETM + visible and near-infrared band data on 28 August 2013 (Hall, Riggs, & Salomonson, 1995; Riggs, Hall, & Salomonson, 1994); a threshold value of 0.67 was used for extracting the Qiyi glacier boundary. Given that the thermal infrared band data have a spatial resolution of 30 m, which has been resampled (Cubic Convolution method) from the original data with a 60 m spatial resolution (https://earth.esa.int/documents/10174/679851/LANDSAT_Products_Description_Document.pdf), we reduced the spatial extent of the glacier boundary by 30 m to remove the influence of this mixed pixel coverage on the glacier boundary in the thermal infrared band data, and to guarantee that the GST retrieval included only the fully covered snow and ice regions of Qiyi glacier.

2.2. Landsat GST retrieval algorithms

2.2.1. Landsat-ETM + data

Landsat-ETM + data were obtained from the USGS website (http://glovis.usgs.gov/), with a pixel resolution of 30 m (for the VNIR/SWIR and the thermal infrared bands). ETM + data spanning a complete hydrologic year (July 2012–September 2013) were employed to retrieve GST (Table 2), thus allowing us to estimate the ability of employing ETM + data to retrieve GST across different seasons.

2.2.2. JM algorithm

The JM algorithm, which is based on the thermal radiation transfer equation, calculates LST from data from only one thermal infrared band with good adaptability to a given study area. We provide only a brief description of the JM algorithm here; specific details on the theory and derivation of this approach can be found in Jiménez-Muñoz and Sobrino (2003); Jiménez-Muñoz et al. (2009).

The thermal radiation transfer equation is expressed as

$$L_\lambda^{at-sensor} = \left[\varepsilon_\lambda B(\lambda, T_S) + (1-\varepsilon_\lambda)L_\lambda^{atm\downarrow}\right]\tau_\lambda + L_\lambda^{atm\uparrow}, \tag{1}$$

where $L_\lambda^{at-sensor}$ is the at-sensor radiance for a given wavelength (λ), ε_λ is the surface emissivity, $B(\lambda, T_S)$ is the radiance emitted by a blackbody at temperature T_S, $L_\lambda^{atm\downarrow}$ is the down-welling radiance, τ_λ is the total transmission of the atmosphere (transmissivity), and $L_\lambda^{atm\uparrow}$ is the up-welling atmospheric radiance.

The JM algorithm consists of a three-step process. Firstly, $B(\lambda, T_S)$ is given by Planck's law. Since a linear relationship between radiance and temperature can be found from the Taylor's approximation around a certain temperature (T_0), $B(\lambda, T_S)$ can be expanded as a function of T_0. The at-sensor brightness temperature ($T_{at-sensor}$) can be chosen as T_0.

The expansion of $B(\lambda, T_S)$ is then substituted in Eq. (1), and three atmospheric functions (ψ_1, ψ_2, and ψ_3) are applied to constrain T_S:

$$T_S = \gamma\left[\varepsilon_\lambda^{-1}\left(\psi_1 L_\lambda^{at-sensor} + \psi_2\right) + \psi_3\right] + \delta, \tag{2}$$
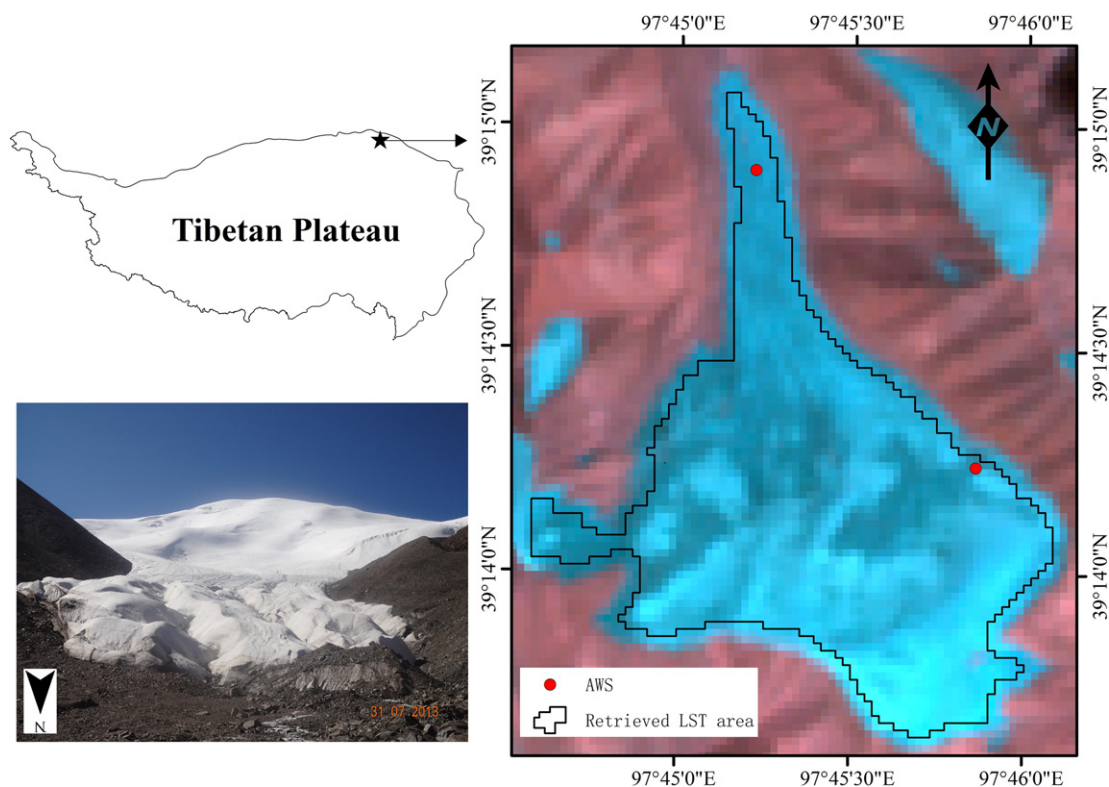
Fig. 1. Location of Qiyi glacier on the northern edge of the Qinghai–Tibetan Plateau. The panel at right shows the RGB image, comprising the 7th, 4th, and 2nd bands of the ETM + collected on 28 August 2013. The bold black lines on the glacier indicate the extent of the remote-sensing-retrieved LST for the glacier and the red dots represent AWS sites.

where

$$\psi_1 = \frac{1}{\tau_\lambda}, \tag{3}$$

$$\psi_2 = -L_\lambda^{atm\downarrow} - \frac{L_\lambda^{atm\uparrow}}{\tau_\lambda}, \tag{4}$$

and

$$\psi_3 = L_\lambda^{atm\uparrow}. \tag{5}$$

Secondly, in Eq. (2), γ and δ are obtained from the linear approximation of Planck's law, given by

$$\gamma = \left\{ \frac{c_2 L_\lambda^{at-sensor}}{T_{at-sensor}^2} \left[\frac{\lambda_{eff}^4}{c_1} L_\lambda^{at-sensor} + \lambda_{eff}^{-1} \right] \right\}^{-1} \tag{6}$$

and

$$\delta = -\gamma L_\lambda^{at-sensor} + T_{at-sensor}, \tag{7}$$

where $T_{at-sensor}$ is the at-sensor brightness temperature, λ_{eff} is the effective wavelength for the thermal infrared channel, and c_1 and c_2

are Planck's law constants; $c_1 = 1.19104 \times 10^8$ W·μm^4/m^2/Sr and $c_2 = 1.43877 \times 10^4$ μm·K.

In the third step, the up- and down-welling atmospheric radiance values are obtained using atmospheric radiative transfer software (MODTRAN4) (Berk et al., 1999), utilizing the atmospheric profile data, water content, and transmissivity as inputs. The relationship matrix between the three atmospheric functions (ψ_1, ψ_2, and ψ_3) and water content (ω) is expressed by the following least-squares fitting approach:

$$\begin{bmatrix} \psi_1 \\ \psi_2 \\ \psi_3 \end{bmatrix} = \begin{bmatrix} c_{11} & c_{12} & c_{13} \\ c_{21} & c_{22} & c_{23} \\ c_{31} & c_{32} & c_{33} \end{bmatrix} \begin{bmatrix} \omega^2 \\ \omega \\ 1 \end{bmatrix}, \tag{8}$$

where the c_{ij} matrix coefficients map this atmosphere–water content relationship. The following matrix coefficients obtained from the TIGR2 (Thermodynamic Initial Guess Retrieval) database are applied to the present LST retrieval because this matrix represents a water vapor content that is similar to that present in the study area.

$$C = \begin{bmatrix} 0.06518 & 0.00683 & 1.02717 \\ -0.53003 & -1.25866 & 0.10490 \\ -0.01965 & 1.36947 & -0.24310 \end{bmatrix} \tag{9}$$

Table 1
Sensor specification for each AWS site.

Sensor type	Data acquisition	Sampling frequency	Spectral range	Accuracy
SI-111	Surface temperature	30 s	8–14 μm	±0.2 °C for −10° to 65 °C
				±0.5 °C for −40° to 70 °C
CNR1	Incoming short-wave radiation	30 s	305–2800 nm	±10%
	Incoming long-wave infrared radiation	30 s	5–50 μm	±10%
	Surface-reflected short-wave radiation	30 s	305–2800 nm	±10%
	Outgoing long-wave infrared radiation	30 s	5–50 μm	±10%

Table 2
Description of the ETM + data, MOD05 data, and ground instrument data.

Date (y/m/d)	Year_Julian Day	ETM + pass time (h/m/s)	MOD05 pass time (h/m)	SI-111 record 4410 m/4470 m	CNT1 record 4410 m/4470 m
2012/7/8	2012_190	12:02:46	12:25	None/yes	None/yes
2012/8/25	2012_238	12:03:18	12:25	Yes/yes	None/yes
2012/9/26	2012_270	12:03:38	12:25	Yes/yes	Yes/yes
2012/10/12	2012_286	12:03:46	12:20	Yes/yes	Yes/yes
2012/10/28	2012_302	12:03:55	12:25	Yes/yes	Yes/yes
2012/11/13	2012_318	12:04:00	12:25	Yes/yes	Yes/yes
2012/11/29	2012_334	12:04:04	12:25	Yes/yes	Yes/yes
2012/12/15	2012_350	12:04:10	12:25	Yes/yes	Yes/yes
2013/1/16	2013_016	12:04:13	12:25	None/yes	None/yes
2013/2/1	2013_032	12:04:18	12:25	None/yes	None/yes
2013/4/6	2013_096	12:04:07	12:25	None/yes	None/yes
2013/4/22	2013_112	12:04:00	12:25	Yes/yes	Yes/yes
2013/5/8	2013_128	12:03:58	12:25	Yes/yes	Yes/yes
2013/5/24	2013_144	12:03:55	12:25	Yes/yes	Yes/yes
2013/8/28	2013_240	12:03:30	12:25	Yes/yes	Yes/yes
2013/9/13	2013_256	12:03:43	12:25	Yes/yes	Yes/none

LST can then be constrained from the remote sensing thermal infrared band data with only two unknown factors, the surface emissivity (ε_λ) and the water vapor content of the atmosphere (ω), by substituting Eqs. (6), (7), and (9) into Eq. (2).

2.2.3. Emissivity algorithms

Previous studies have revealed that snow emissivity is a function of snow grain size and exitance angle (Hori et al., 2006; Rees & James, 1992; Wald, 1994). Hori et al. (2013) developed a semi-empirical model for the angular-dependent emissivity spectra of snow and ice in the 8–14 μm atmospheric window. Based on field observations, Hori et al. (2013) classified the transition from snow to ice into five categories: fine dendrite snow ($f_{sp} = 0.22$, where f_{sp} is the weighting parameter, which is explained in the following equations), medium granular snow ($f_{sp} = 0.29$), coarse-grained snow ($f_{sp} = 0.41$), sun crust ($f_{sp} = 0.53$), and bare ice ($f_{sp} = 0.95$). They assumed that emissivity of the snow/ice surface could be expressed by a weighted sum of emissivity components: those of both the specular and blackbody surfaces. This is expressed by a linear combination of emissivities for the specular and blackbody surfaces, with a weighting parameter characterizing the specularity of the bulk surface:

$$\varepsilon_{snow}(\lambda,\ \theta) = \varepsilon_{bb}(\lambda)\left(1 - f_{sp}\right) + \varepsilon_{sp\_app}(\lambda,\ \theta)f_{sp}, \tag{10}$$

$$\varepsilon_{sp\_app}(\lambda,\ \theta) = \varepsilon_{sp}(\lambda,\ 45^\circ)\left(1 - f_{sp}\right) + \varepsilon_{sp}(\lambda,\ \theta)f_{sp}, \tag{11}$$

and

$$\varepsilon_{sp}(\lambda,\ \theta) = 1 - \rho_{sp}(\lambda,\ \theta), \tag{12}$$

where λ is the wavelength, θ is the angle of exitance measured from the normal, $\varepsilon_{snow}(\lambda,\ \theta)$ is the angular-dependent emissivity of snow, $\varepsilon_{bb}(\lambda)$ is the emissivity of the isotropic blackbody ($\varepsilon_{bb}(\lambda) = 1$), $\varepsilon_{sp\_app}(\lambda,\ \theta)$ is the apparent emissivity of the specular fraction, $\varepsilon_{sp}(\lambda,\ \theta)$ is the emissivity of an ideal smooth ice surface simulated with the Fresnel reflectance $\rho_{sp}(\lambda,\ \theta)$, and f_{sp} is the weighting parameter, indicating an effective areal fraction of specular surface within the overall surface. In addition, Eq. (12) follows Kirchhoff's law; the details can be found in Hori et al. (2013). Here we calculated the exitance angle θ for every pixel, based on GDEM data and the relative position between the ETM + sensor and Qiyi glacier. ETM + VNIR/SWIR band data, as well as simultaneous thermal infrared band data, were used to characterize the glacier surface.

During the glacier-surface classification procedure, we also took into account atmospheric and topographic influences. After applying the FLAASH atmospheric correction (Luo, Chen, & Le, 2008), we compared several topographic correction algorithms, but none provided a satisfactory result, as they either suffered from overcorrection problems or introduced new errors. Therefore, we utilized the band ratio approach to eliminate the impact of topography as much as possible (Albert, 2002; Hall, Foster, & Chang, 1992; Pope & Rees, 2014), which also benefited the discrimination between different snow grains (Bronge & Bronge, 1999; Fily, Bourdelles, Dedieu, & Sergent, 1997). Three types of band ratio images (i.e., NDSI, band3/band5, and band4/band5) were chosen to classify the transient state from snow to ice. They were standardized over the range 0–255 and stacked together. Next, they were classified using the K-Mean unsupervised classification method (Barcaza, Aniya, Matsumoto, & Aoki, 2009; König et al., 2004; Pope & Rees, 2014), combined with the results of previous field investigations and the color/brightness information from the corresponding RGB image being composed by the 7th, 4th, and 2nd band, into six categories: fine dendrite snow ($f_{sp} = 0.22$), medium granular snow ($f_{sp} = 0.29$), coarse-grained snow ($f_{sp} = 0.41$), sun crust ($f_{sp} = 0.53$), bare ice ($f_{sp} = 0.95$), and water. In this approach the emissivity of water has a fixed value of 0.9885 (Lamaro, Mariñelarena, Torrusio, & Sala, 2013; Simon, Tormos, & Danis, 2014). Field observations of Qiyi glacier are carried out monthly, while from June to September observations are made every five days. These field experiences are then used to assign snow types for unsupervised classification results. The snow cover types and calculated emissivity values for Qiyi glacier are provided in Figs. S1 and S2 of the Supplementary data, respectively. Owing to the lack of observations at the same time as satellite pass times in the field, we cannot evaluate the K-Mean classification results quantitatively. However, we can use the albedo of different types of snow/ice to verify our classification results. Here, we utilize the observation data of the AWS on the Qiyi Glacier to calculate the albedo of different types of snow/ice by the K-Mean classification method (Fig. 2). The results illustrate clearly that the albedo of the fine dendrite snow is close to 1, and the albedos of the other types of aged snow decrease gradually, and the albedo of glacial bare ice is the minimum (only about 0.2). Those are identical with observations of snow/ice albedo (Cuffey & Paterson, 2010), which implies that the classification results in this paper are reliable.

2.2.4. MODIS water vapor content data

The water vapor content data utilized here are from the Total Perceptible Water product (MOD05), which was obtained from the Moderate Resolution Imaging Spectroradiometer (MODIS). For details of the calculation method, see Gao and Kaufman (2003). MOD05 data have been evaluated previously by analyzing in situ measurements of vegetation, urban areas, and other surfaces (Chen, Huang, & Jackson, 2005; Sobrino, El Kharraz, & Li, 2003; Zarco-Tejada, Rueda, & Ustin,
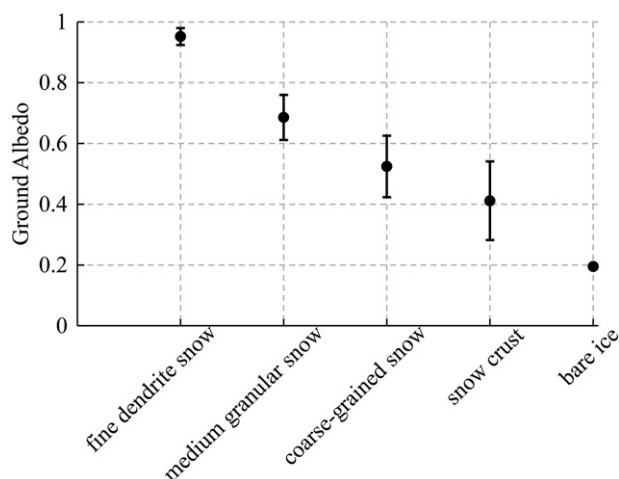
Fig. 2. Albedo of the different snow/ice types at the AWS site on the Qiyi Glacier, July 2012 to September 2013.

have a much coarser spatial resolution (1 km) than the ETM + thermal infrared data (30 m), a linear correlation between the MOD05 image pixel values and their corresponding mean elevations (obtained by superimposing the MOD05 images onto the GDEM image) was used to interpolate the coarser MOD05 water concentration data onto the 30-m pixel size by using the GDEM dataset with a spatial resolution of 30 m (Fig. 3). A few extrapolated pixels have values below zero, which is impossible in reality; here we assigned these pixels with a value of 0.00001. It should be noted that the MOD05 water vapor content data had error bands that needed to be eliminated (these error bands are shown in Fig. S3 of the Supplementary data). The calculated total water vapor content for the study area ranged from 0.00001 to 0.83 g/cm² from July 2012 to September 2013 (Fig. S4 of the Supplementary data).

2.3. Ground GST data

Two AWSs are used to validate the remote-sensing-derived GSTs in this study (Fig. 1). One AWS is situated on the glacier tongue at an elevation of 4410 m, which is located in the ablation zone of Qiyi glacier. The other AWS is located on the upper part of the glacier at an elevation of 4770 m, within the accumulation zone. However, recent mass balance measurements using stakes highlight a negative mass balance, suggesting that this AWS site may now be in an ablation zone.

2.3.1. Ground instrument and ground GST estimation

SI-111 radiometers and CNR1 net radiometers were used to calculate GST. These instruments were installed 1.5 m above the surface at the two AWSs. The SI-111 sensor has a field of view with a half-angle of 22°. Samples were taken every 30 s and then averaged to obtain 10-min values that were archived on a Campbell CR1000 data logger.
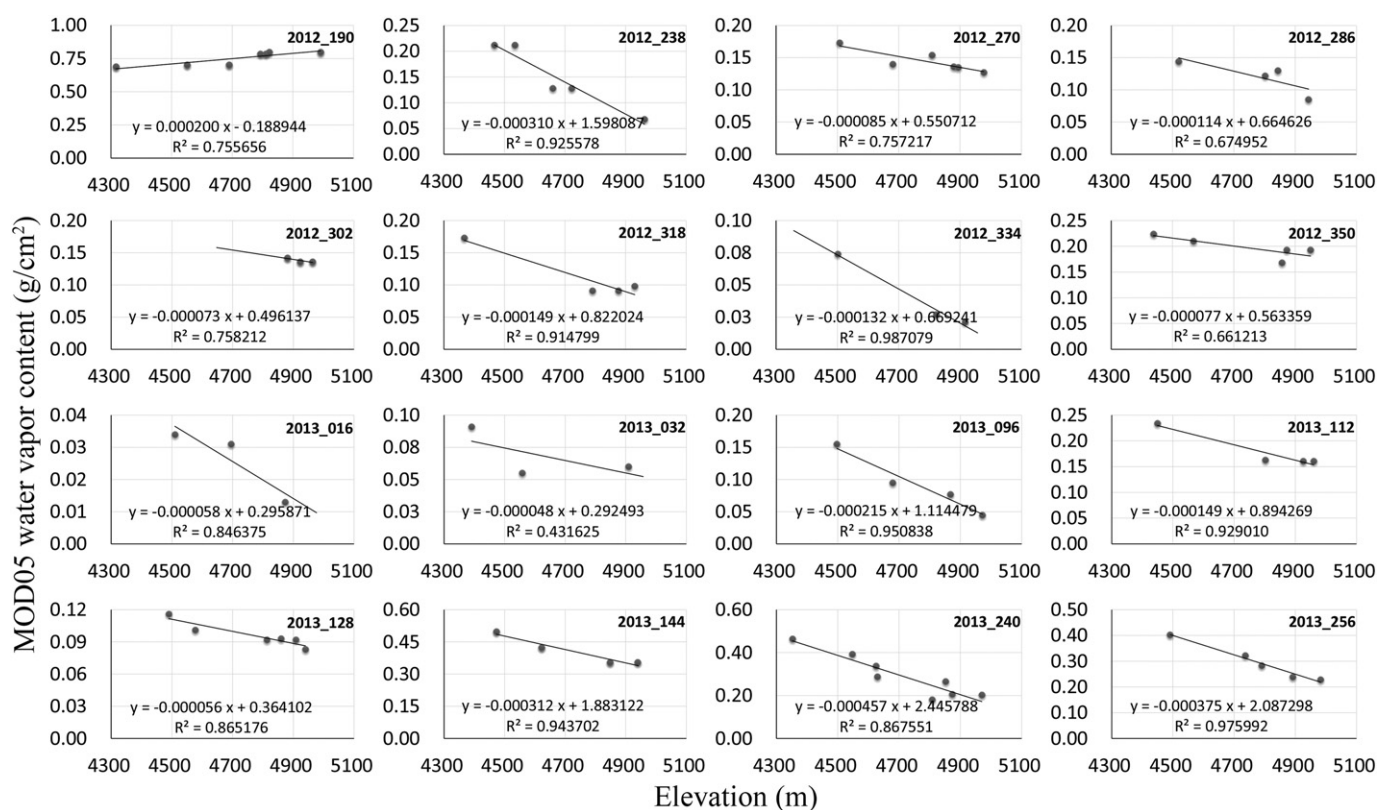
2003), and Chen, Zhao, Ye, and Hu (2011) suggested that the MOD05 data can be applied to LST retrieval, using Landsat thermal infrared data. However, the applicability of such data to glaciers has not been previously evaluated, as glaciers possess a very different underlying surface. Since the pass time of the ETM + data occurred between 12:03 and 12:04 (GMT +8 time zone) at present study area, while the data-collection time of the MOD05 was about 12:25, we assumed that the water vapor content was unchanged during this time span and that the vapor product yielded true values. Since the MOD05 data

Fig. 3. MOD05 water vapor content (g/cm²) versus corresponding mean elevations for different satellite passes from July 2012 to September 2013. The best linear fit (solid lines) for each of the 16 passes during the 2012–2013 hydrologic year is shown (dates in Year_Julian Day format).

The radiometric temperatures measured by the SI-111 radiometer were corrected for emissivity and the CNR1 downward sky irradiance effects. The GST T_s is given by

$$B(T_s) = \left[B(T_r) - (1-\varepsilon)L_{sky} \right]/\varepsilon, \qquad (13)$$

where B is the Planck function weighted for the spectral response function of the SI-111 radiometer, T_r is the radiometric temperature measured by the SI-111 radiometer, ε is the surface emissivity obtained following Hori et al. (2013), and L_{sky} is the downward sky irradiance divided by π. Note that the SI-111 radiometers and CNR1 net radiometers were not working normally for the entire period because of the hostile environment of the glacier; the available instrument records are listed in Table 1.

2.3.2. Ground GST uncertainty

The ground measurement GST uncertainties $\delta(T_s)$ include calibration, emissivity correction, temporal, and spatial uncertainties (Li et al., 2014; Niclòs, Galve, Valiente, Estrela, & Coll, 2011), which can be expressed as follows:

$$\delta(T_s) = \left[\delta(cal)^2 + \delta(emis)^2 + \delta(temp)^2 + \delta(spat)^2 \right]^{1/2}. \qquad (14)$$

The absolute accuracy of SI-111 radiometers is ± 0.2 K at -10 to $+65$ °C, and ± 0.5 K at -40 to $+70$ °C (the quoted factory specifications; http://www.apogeeinstruments.com/infraredradiometer). The precision of the CNR1 net radiometers is $\pm 10\%$, with a negligible influence on GST (<0.02 K) (Eq. (13)). The emissivity of the measured GST values has been corrected to be the same as that from the remote-sensing-retrieved GST values, meaning that the emissivity uncertainties will have a minimal effect on the differences between measured and retrieved GST. Because the remote sensing images captured the instant temperature on the glacier surface, whereas the ground measurements provided 10-min mean values spanning the satellite pass time, and because the complex topography of the mountain glacier will result in a spatially heterogeneous temperature distribution, we only compared the 10-min mean values with retrieved GSTs from the corresponding pixels at the two AWSs. Given this, we defined the instrumental calibration errors as the spatiotemporal GST uncertainties when comparing the remote-sensing-retrieved GST values with 10-min mean GST values spanning the satellite overpass time.

3. Results

The retrieved GSTs from the ETM+ thermal infrared band were compared with the field-measured GSTs (Fig. 4) to validate the accuracy of the remote-sensing-retrieved GST values. The limited sample size of the field measurements was insufficient for us to assess the seasonal influences on the errors of the retrieved GSTs. Therefore, we analyzed their accuracies over the entire study period (one hydrologic year) to minimize seasonal variability. During the July 2012–September 2013 time period, 26 pairs of remote-sensing-retrieved and measured GSTs were compared. The mean deviation of the remote-sensing-retrieved temperature was -0.96 K when compared with the measurements, the standard deviation of the differences between retrieved and measured GST was 1.18 K, and the root mean square error (RMSE) was 1.50 K. A scatter plot of the data shows that when the ground GST was negative (<273.15 K), the remote-sensing-retrieved GST was generally lower than the ground measurements; when the surface temperature was positive (>273.15 K), the remote-sensing-retrieved temperatures tend to be overestimated (Fig. 4).

The remote-sensing-retrieved temperature distribution on the entire glacier shows that even though the surface temperature generally decreases with increasing altitude (Fig. 5), the lowest temperatures are not at the highest altitudes of the glacier because the local topography
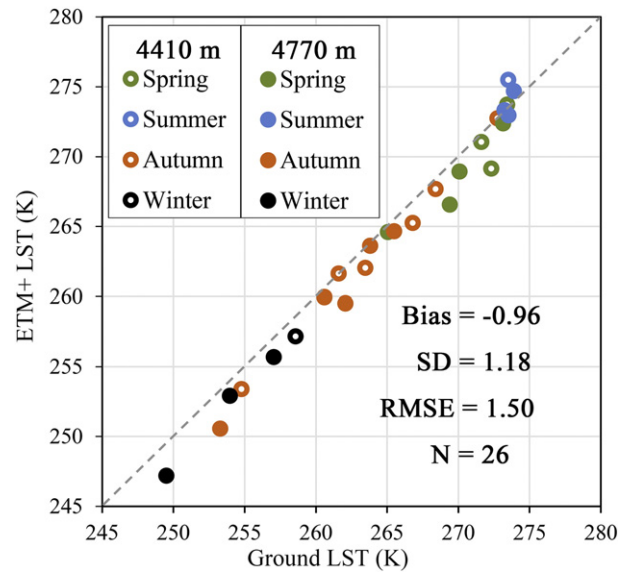

Fig. 4. ETM+ remote-sensing-retrieved GSTs versus surface GST measurements at the 4410 m AWS site (open circles) and 4770 m AWS site (filled circles).

also influences surface temperature. It is noteworthy that some of the pixels in the glacier tongue yielded temperatures larger than 275 K in the 2012_190, 2012_238, 2013_144, and 2013_240 satellite passes. However, all the field measurement records show that the maximum temperature is 275.0 K (at 4410 m AWS site) and 274.6 K (at 4770 m AWS site) during the 2012–2013 hydrologic year. We infer that the GST of these pixels larger than 275.0 K might be overestimated, which will be further discussed in Section 4.4.

4. Discussion

4.1. Sensitivity analysis of emissivity to surface exitance angle

Hori et al. (2013) compared the modeled emissivity spectra and the in situ measured spectra in 8–14 μm for five categories from snow to ice and six fixed exitance angles (0°, 15°, 30°, 45°, 60°, and 75°). Here, we analyzed the variations in emissivity, particularly on the ETM+ thermal infrared band spectrum range (10.40–12.50 μm), with a surface exitance angle ranging from 0° to 75° (Fig. 6). As the exitance angle increases, the emissivity of all five snow and ice categories exhibits an exponential decay. This decay is slowest for fine dendrite snow, with an emissivity decrease of only 0.01, whereas the emissivity of bare ice is the most sensitive to exitance angle, with an emissivity decrease of >0.01 at $\theta = 46°$ that decreases by 0.20 at $\theta = 75°$. The sensitivity of emissivity to exitance angle for the other three categories lies in between that of fine dendrite snow and bare ice.

4.2. Sensitivity analysis of GST to emissivity

The radiance of the ETM+ thermal infrared band data from July 2012 to September 2013 varies from 3.33 to 6.68 W/m^2·sr·μm after calibration, and the emissivity range is 0.963 to 0.993, as obtained from the Hori model simulation. Those curves with radiance values of 6.68 and 3.33 W/m^2·sr·μm can be characterized as Group 1 and Group 2, respectively. Variations in the GST bias with emissivity variations from 0.96 to 1 were analyzed for a range of water vapor concentrations for the two groups (we divided water vapor content on Qiyi glacier into 11 grades from 0.01 to 0.9 g/cm^2), and the results show that the emissivity has a linear relationship with the resultant temperature bias ($R > 0.99$) (Fig. 7). It seems that when the glacier surface was warmer (Group 1), errors in temperature driven by the emissivity error were much greater than the errors associated with the lower-temperature
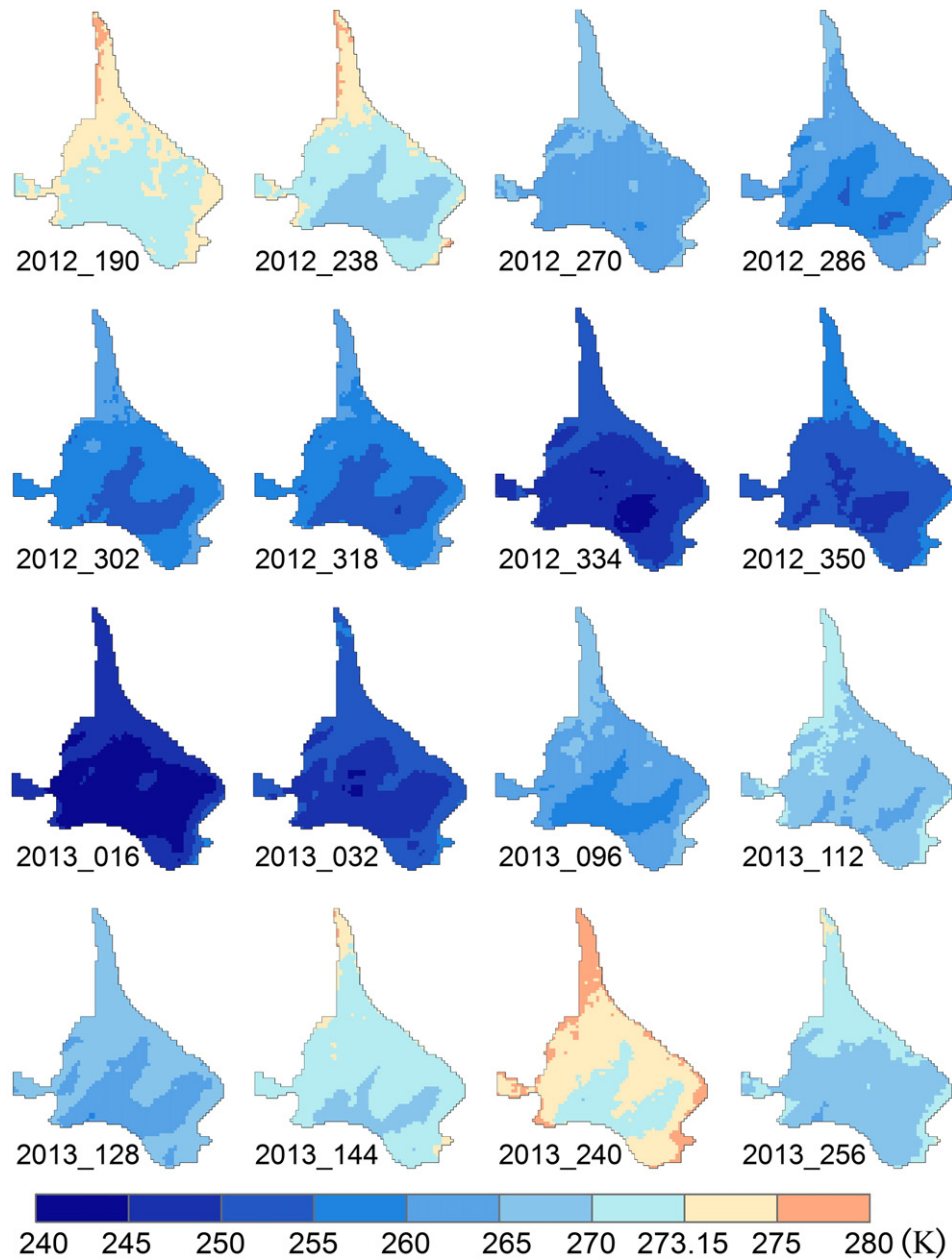
Fig. 5. Distribution of remote-sensing-derived GST across Qiyi glacier from July 2012 to September 2013. The 16 Landsat passes during the 2012–2013 hydrologic year are shown (dates in Year_Julian Day format).

case (Group 2). For example, when the glacier surface was warmer (i.e., the radiance was 6.68 W/m^2·sr·μm; Group 1) and with the lowest water vapor content (0.01 g/cm^2), the temperature bias was as large as +0.65 K (−0.65 K), with an underestimate (overestimate) of 0.01 in emissivity. By comparison, when the glacier was colder (i.e., the radiance is 3.33 W/m^2·sr·μm; Group 2) and with the highest water vapor content (0.9 g/cm^2), the temperature bias was at a minimum value +0.30 K (−0.30 K), with an underestimate (overestimate) of 0.01 in emissivity.

4.3. Sensitivity analysis of GST to water content

Variations in the temperature bias with water vapor contents from 0.01 to 0.9 g/cm^2 were analyzed at different emissivity grades for the two groups, and the emissivity was classified into five grades from 0.96 to 1 (Fig. 8). The results show that when the glacier was warmer (Group 1), each change in water vapor concentration of 0.10 g/cm^2

resulted in minor variations in the temperature differences at all emissivity grades, with a maximum bias of 0.11 K when the water vapor concentration was near 0.2 g/cm^2. In contrast, when the glacier surface was colder (Group 2) and the water vapor concentration was <0.3 g/cm^2, the temperature bias at each water vapor change of 0.1 g/cm^2 was always <0.11 K, regardless of emissivity grade. However, when the water vapor concentration was >0.3 g/cm^2, the resultant temperature bias of 0.1 g/cm^2 water vapor increased continuously with increasing water vapor concentration, and the temperature bias reached 0.72 K with a water vapor concentration of 0.9 g/cm^2 (when the water vapor concentration was overestimated by 0.1 g/cm^2).

4.4. Sources of errors in retrieved GST on mountain glaciers

Fig. 3 shows that when the glacier surface is colder, the water vapor concentration remains lower and is ≤0.25 g/cm^2, which will produce a relatively small LST difference (Group 2 in Fig. 8). When the glacier
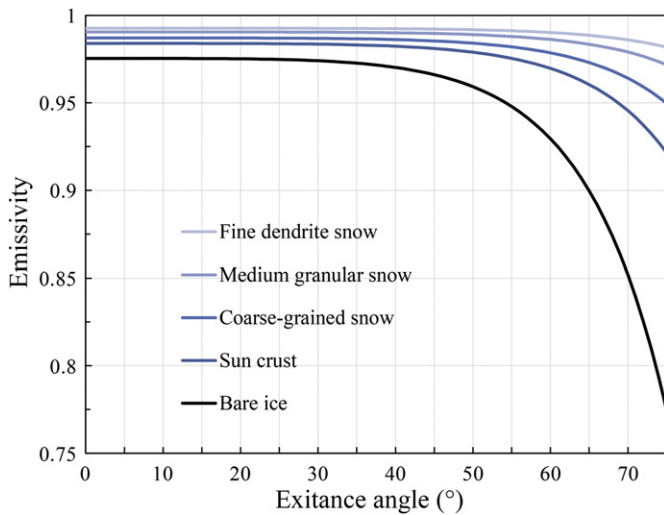
Fig. 6. Variations in emissivity integrated over the ETM+ thermal infrared band spectrum range (10.40–12.50 μm) with exitance angle for different types of snow and ice.

Fig. 8. Variations in the retrieved temperature biases with water vapor concentration for the two groups and different emissivities. The curves with radiance values of 6.68 and 3.33 W/m²·sr·μm correspond to the Group 1 and Group 2 variations, respectively.

surface is warmer, the water vapor concentration may change from 0.01 to 0.83 g/cm² (Fig. 3), and the resultant LST differences are even smaller (Group 1 in Fig. 8). Therefore, for the JM algorithm, the influence of water vapor concentration errors on the retrieved GST bias is smaller than emissivity errors for Qiyi glacier. We have adopted the snow type classification strategy and emissivity model proposed by Hori et al. (2013) and applied it to Qiyi glacier; however, this glacier's surface has its own unique characteristics. For example, bare ice contains many cryoconite holes during the summer melt season, which may affect the accuracy of the LST retrieval proposed in this study.

Although the RMSE is only 1.50 K when comparing the remote-sensing-retrieved GST with the observations at the two AWS sites, the retrieved GST spatial patterns (Fig. 5) show that during the summer (e.g., 2012_190, 2012_238, and 2013_240), the errors in remote-sensing-retrieved surface temperature on the glacier tongue and some glacier marginal area are larger than the errors at the two AWS sites. We infer that these temperature anomalies arise from the overvalued radiance on ETM+ thermal infrared band data at both areas. Though the entire glacier surface is affected by thermal emissions from the surrounding topography (Hock, 2005; Proy, Tanre, & Deschamps, 1989; Strasser et al., 2004), the magnitude of this effect is influenced

by the distance between surrounding mountains and the glacier itself (Proy et al., 1989). For example, the reflection of thermal energy emitted from adjacent topography is greater at the glacier margins and on the glacier tongue than in the center of the glacier, owing to the shorter distances involved and decreased atmospheric absorption. Furthermore, this effect is amplified during the summer, when bare rock surfaces bordering the glacier have higher temperatures than during the winter.

In the present study, all of the thermal data were calibrated by the USGS using the latest Calibration Parameter File (CPF). The thermal band radiometric calibration bias error of ETM+ introduces an expected uncertainty of 0.48 K in retrieved GST on mountain glaciers (Schott et al., 2012).

5. Conclusions

By employing the ETM+ thermal infrared band dataset and the water vapor content data of MOD05, the GST distribution across Qiyi glacier was calculated by coupling the JM algorithm to an emissivity model that considers the exitance angle. The remote-sensing-derived glacier surface temperatures are validated by the 10-min mean in situ measurements at two AWS sites, and the results show reasonable accuracy at the two sites, with a mean bias of 0.96 K and a mean RMSE of 1.5 K, which indicate that the source data and method applied to Qiyi glacier are practical, except for the glacier marginal area and the glacier tongue. However, we believe that four major aspects need to be improved to obtain more accurate remote-sensing-derived GST, as follows.

(1) In this study we have adopted the snow type classification strategy proposed by Hori et al. (2013) and applied it to Qiyi glacier; however, this glacier's surface has its own unique characteristics. Therefore, field measurements are required to validate the emissivity model for this glacier. (2) Variations in the water vapor content on the glacier may not conform to the dataset used in the JM algorithm. Therefore, we should develop specific parameters between the atmospheric functions (ψ_1, ψ_2, and ψ_3) and water content (ω) that are more applicable to GST retrieval. (3) In the glacier tongue and the glacier marginal area, reflection of thermal emissions from adjacent mountain slopes, rather than the atmosphere, is dependent on topography and the specularity of the glacier surface itself (Hock, 2005; Proy et al., 1989; Strasser et al., 2004). Consequently, this effect needs to be accounted for in satellite-based estimates of radiance. (4) A sound placement strategy of instruments for ground measurements of GST and a higher temporal
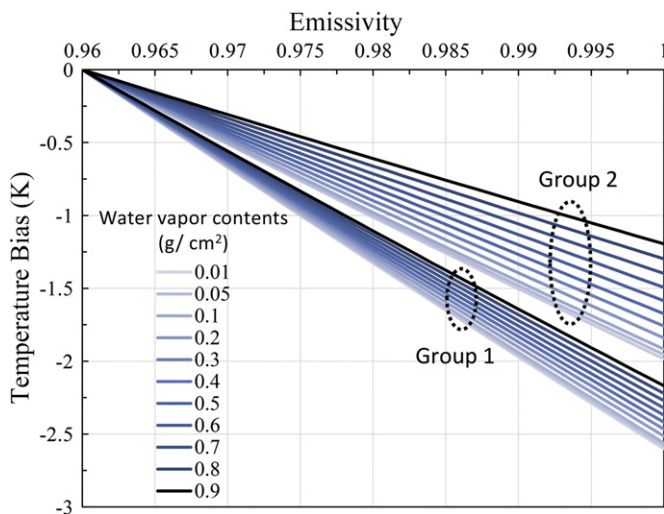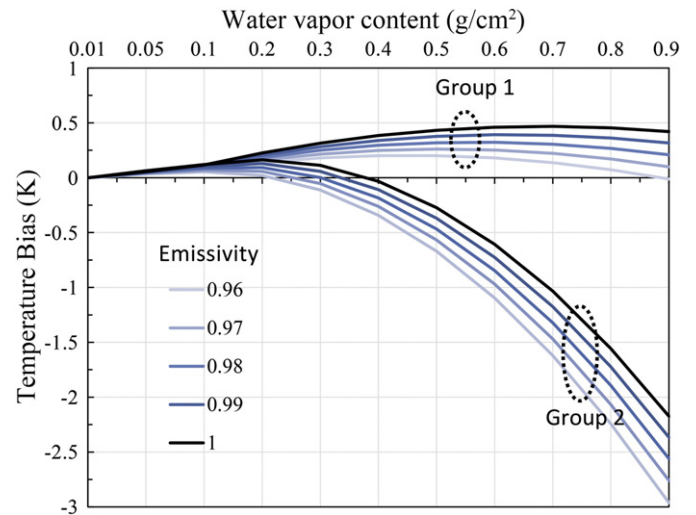

Fig. 7. Variations in the retrieved GST biases with emissivity for the two groups with different water vapor concentrations. The curves with the radiance values of 6.68 and 3.33 W/m²·sr·μm correspond to the Group 1 and Group 2 variations, respectively.

resolution of ground measurement records are necessary to evaluate remote-sensing-retrieved GST results more effectively.

Acknowledgments

Appendix A. Supplementary data

Supplementary data associated with this article can be found in the online version, at http://dx.doi.org/10.1016/j.rse.2015.03.026. These data include Google map of the most important areas described in this article.

References

Albert, T. H. (2002). Evaluation of remote sensing techniques for ice-area classification applied to the tropical Quelccaya Ice Cap, Peru. *Polar Geography, 26*, 210–226.

Anderson, M., Kustas, W., Norman, J., Hain, C., Mecikalski, J., Schultz, L., et al. (2011). Mapping daily evapotranspiration at field to continental scales using geostationary and polar orbiting satellite imagery. *Hydrology and Earth System Sciences, 15*, 223–239.

Anderson, M., Norman, J., Diak, G., Kustas, W., & Mecikalski, J. (1997). A two-source time-integrated model for estimating surface fluxes using thermal infrared remote sensing. *Remote Sensing of Environment, 60*, 195–216.

Anderson, M., Norman, J., Kustas, W., Houborg, R., Starks, P., & Agam, N. (2008). A thermal-based remote sensing technique for routine mapping of land-surface carbon, water and energy fluxes from field to regional scales. *Remote Sensing of Environment, 112*, 4227–4241.

Anul Haq, M., Jain, K., & Menon, K. (2012). Surface temperature estimation of Gangotri Glacier using thermal remote sensing. *ISPRS—International Archives of the Photogrammetry, Remote Sensing and Spatial Information Sciences, 1*, 115–119.

Arnold, N., Willis, I., Sharp, M., Richards, K., & Lawson, W. (1996). A distributed surface energy-balance model for a small valley glacier. I. Development and testing for Haut Glacier d'Arolla, Valais, Switzerland. *Journal of Glaciology, 42*, 77–89.

Barcaza, G., Aniya, M., Matsumoto, T., & Aoki, T. (2009). Satellite-derived equilibrium lines in Northern Patagonia Icefield, Chile, and their implications to glacier variations. *Arctic, Antarctic, and Alpine Research, 41*, 174–182.

Barsi, J. A., Barker, J. L., & Schott, J. R. (2003). An atmospheric correction parameter calculator for a single thermal band earth-sensing instrument. *Geoscience and Remote Sensing Symposium, 2003. IGARSS'03. Proceedings. 2003 IEEE International* (pp. 3014–3016). IEEE.

Becker, F., & Li, Z. -L. (1990). Towards a local split window method over land surfaces. *Remote Sensing, 11*, 369–393.

Berk, A., Anderson, G., Acharya, P., Chetwynd, J., Bernstein, L., Shettle, E., et al. (1999). *MODTRAN4 User's Manual.* Hanscom AFB, MA, 01731-03010: Air Force Research Laboratory, Space Vehicles Directorate, Air Force Materiel Command.

Bronge, L. B., & Bronge, C. (1999). Ice and snow-type classification in the Vestfold Hills, East Antarctica, using Landsat-TM data and ground radiometer measurements. *International Journal of Remote Sensing, 20*, 225–240.

Brunsell, N. A., & Gillies, R. R. (2003). Length scale analysis of surface energy fluxes derived from remote sensing. *Journal of Hydrometeorology, 4*, 1212–1219.

Chen, D., Huang, J., & Jackson, T. J. (2005). Vegetation water content estimation for corn and soybeans using spectral indices derived from MODIS near-and short-wave infra-red bands. *Remote Sensing of Environment, 98*, 225–236.

Chen, F., Zhao, X., Ye, H., & Hu, H. (2011). Retrieving land surface temperature from Landsat TM using different atmospheric products as ancillary data. *Spatial Data Mining and Geographical Knowledge Services (ICSDM), 2011 IEEE International Conference on* (pp. 421–426). IEEE.

Comiso, J. C. (2000). Variability and trends in Antarctic surface temperatures from in situ and satellite infrared measurements. *Journal of Climate, 13*, 1674–1696.

Comiso, J. C. (2006). Arctic warming signals from satellite observations. *Weather, 61*, 70–76.

Cuffey, K. M., & Paterson, W. S. B. (2010). The Physics of Glaciers (4th ed.). Elsevier, 145–147.

Dyurgerov, M. B., & Meier, M. F. (1997). Year-to-year fluctuations of global mass balance of small glaciers and their contribution to sea-level changes. *Arctic and Alpine Research*, 392–402.

Dyurgerov, M. B., & Meier, M. F. (2000). Twentieth century climate change: Evidence from small glaciers. *Proceedings of the National Academy of Sciences, 97*, 1406–1411.

Fily, M., Bourdelles, B., Dedieu, J., & Sergent, C. (1997). Comparison of in situ and Landsat Thematic Mapper derived snow grain characteristics in the Alps. *Remote Sensing of Environment, 59*, 452–460.

Gao, B. C., & Kaufman, Y. J. (2003). Water vapor retrievals using moderate resolution imaging spectroradiometer (MODIS) near-infrared channels. *Journal of Geophysical Research — Atmospheres (1984–2012), 108*.

Gardner, A. S., Moholdt, G., Cogley, J. G., Wouters, B., Arendt, A. A., Wahr, J., et al. (2013). A reconciled estimate of glacier contributions to sea level rise: 2003 to 2009. *Science, 340*, 852–857.

Gillespie, A. R., Abbott, E. A., Gilson, L., Hulley, G., Jiménez-Muñoz, J. -C., & Sobrino, J. A. (2011). Residual errors in ASTER temperature and emissivity standard products AST08 and AST05. *Remote Sensing of Environment, 115*, 3681–3694.

Gillespie, A., Rokugawa, S., Matsunaga, T., Cothern, J. S., Hook, S., & Kahle, A. B. (1998). A temperature and emissivity separation algorithm for Advanced Spaceborne Thermal Emission and Reflection Radiometer (ASTER) images. *IEEE Transactions on Geoscience and Remote Sensing, 36*, 1113–1126.

Gurgiser, W., Marzeion, B., Nicholson, L, Kaser, G., & Ortner, M. (2013). Modeling energy and mass balance of Shallap Glacier, Peru. *Cryosphere Discussions, 7*.

Hall, D. K., Box, J. E., Casey, K. A., Hook, S. J., Shuman, C. A., & Steffen, K. (2008). Comparison of satellite-derived and in-situ observations of ice and snow surface temperatures over Greenland. *Remote Sensing of Environment, 112*, 3739–3749.

Hall, D. K., Comiso, J. C., DiGirolamo, N. E., Shuman, C. A., Box, J. E., & Koenig, L. S. (2013). Variability in the surface temperature and melt extent of the Greenland ice sheet from MODIS. *Geophysical Research Letters, 40*, 2114–2120.

Hall, D. K., Comiso, J. C., DiGirolamo, N. E., Shuman, C. A., Key, J. R., & Koenig, L. S. (2012). A satellite-derived climate-quality data record of the clear-sky surface temperature of the Greenland ice sheet. *Journal of Climate, 25*, 4785–4798.

Hall, D., Foster, J., & Chang, A. (1992). Reflectance of snow measured in situ and from space in sub-Arctic areas in Canada and Alaska. *IEEE Transactions on Geoscience and Remote Sensing, 30*, 634–637.

Hall, D. K., Riggs, G. A., & Salomonson, V. V. (1995). Development of methods for mapping global snow cover using moderate resolution imaging spectroradiometer data. *Remote Sensing of Environment, 54*, 127–140.

Hock, R. (1999). A distributed temperature-index ice- and snowmelt model including potential direct solar radiation. *Journal of Glaciology, 45*, 101–111.

Hock, R. (2003). Temperature index melt modelling in mountain areas. *Journal of Hydrology, 282*, 104–115.

Hock, R. (2005). Glacier melt: A review of processes and their modelling. *Progress in Physical Geography, 29*, 362–391.

Hock, R., Jansson, P., & Braun, L. N. (2005). *Modelling the response of mountain glacier discharge to climate warming.* Global Change and Mountain Regions. Springer, 243–252.

Hook, S. J., Gabell, A. R., Green, A. A., & Kealy, P. S. (1992). A comparison of techniques for extracting emissivity information from thermal infrared data for geologic studies. *Remote Sensing of Environment, 42*, 123–135.

Hori, M., Aoki, T., Tanikawa, T., Hachikubo, A., Sugiura, K., Kuchiki, K., et al. (2013). Modeling angular-dependent spectral emissivity of snow and ice in the thermal infrared atmospheric window. *Applied Optics, 52*, 7243–7255.

Hori, M., Aoki, T., Tanikawa, T., Motoyoshi, H., Hachikubo, A., Sugiura, K., et al. (2006). In-situ measured spectral directional emissivity of snow and ice in the 8–14 μm atmospheric window. *Remote Sensing of Environment, 100*, 486–502.

Hulley, G., Hook, S., & Baldridge, A. (2008). ASTER land surface emissivity database of California and Nevada. *Geophysical Research Letters, 35*.

Huss, M., Farinotti, D., Bauder, A., & Funk, M. (2008). Modelling runoff from highly glacierized alpine drainage basins in a changing climate. *Hydrological Processes, 22*, 3888–3902.

Jacob, T., Wahr, J., Pfeffer, W. T., & Swenson, S. (2012). Recent contributions of glaciers and ice caps to sea level rise. *Nature, 482*, 514–518.

Jiang, X., Wang, N., He, J., Wu, X., & Song, G. (2010). A distributed surface energy and mass balance model and its application to a mountain glacier in China. *Chinese Science Bulletin, 55*, 2079–2087.

Jiménez-Muñoz, J. C., Cristóbal, J., Sobrino, J. A., Sòria, G., Ninyerola, M., & Pons, X. (2009). Revision of the single-channel algorithm for land surface temperature retrieval from Landsat thermal-infrared data. *IEEE Transactions on Geoscience and Remote Sensing, 47*, 339–349.

Jiménez-Muñoz, J. C., & Sobrino, J. A. (2003). A generalized single-channel method for retrieving land surface temperature from remote sensing data. *Journal of Geophysical Research — Atmospheres (1984–2012), 108*.

Karnieli, A., Agam, N., Pinker, R. T., Anderson, M., Imhoff, M. L., Gutman, G. G., et al. (2010). Use of NDVI and land surface temperature for drought assessment: Merits and limitations. *Journal of Climate, 23*, 618–633.

Kealy, P. S., & Hook, S. J. (1993). Separating temperature and emissivity in thermal infrared multispectral scanner data: Implications for recovering land surface temperatures. *IEEE Transactions on Geoscience and Remote Sensing, 31*, 1155–1164.

Kerr, Y. H., Lagouarde, J. P., & Imbernon, J. (1992). Accurate land surface temperature retrieval from AVHRR data with use of an improved split window algorithm. *Remote Sensing of Environment, 41*, 197–209.

Kerr, Y. H., Lagouarde, J. P., Nerry, F., & Ottlé, C. (2004). *Land surface temperature retrieval techniques and applications.* Thermal Remote Sensing in Land Surface Processes. Boston, USA: CRC Press, 33–109.

Koenig, L. S., & Hall, D. K. (2010). Comparison of satellite, thermochron and air temperatures at Summit, Greenland, during the winter of 2008/09. *Journal of Glaciology, 56*, 735–741.

König, M., Winther, J. -G., Kohler, J., & König, F. (2004). Two methods for firn-area and mass-balance monitoring of Svalbard glaciers with SAR satellite images. *Journal of Glaciology, 50*, 116–128.

Kustas, W., & Anderson, M. (2009). Advances in thermal infrared remote sensing for land surface modeling. *Agricultural and Forest Meteorology*, *149*, 2071–2081.

La Frenierre, J., & Mark, B. G. (2014). A review of methods for estimating the contribution of glacial meltwater to total watershed discharge. *Progress in Physical Geography*, *38*, 173–200.

Lamaro, A. A., Mariñelarena, A., Torrusio, S. E., & Sala, S. E. (2013). Water surface temperature estimation from Landsat 7 ETM+ thermal infrared data using the generalized single-channel method: Case study of Embalse del Río Tercero (Córdoba, Argentina). *Advances in Space Research*, *51*, 492–500.

Li, Z. -L., & Becker, F. (1993). Feasibility of land surface temperature and emissivity determination from AVHRR data. *Remote Sensing of Environment*, *43*, 67–85.

Li, H., Sun, D., Yu, Y., Wang, H., Liu, Y., Liu, Q., et al. (2014). Evaluation of the VIIRS and MODIS LST products in an arid area of Northwest China. *Remote Sensing of Environment*, *142*, 111–121.

Li, Z. -L., Tang, B. -H., Wu, H., Ren, H., Yan, G., Wan, Z., et al. (2013a). Satellite-derived land surface temperature: Current status and perspectives. *Remote Sensing of Environment*, *131*, 14–37.

Li, Z. -L., Wu, H., Wang, N., Qiu, S., Sobrino, J. A., Wan, Z., et al. (2013b). Land surface emissivity retrieval from satellite data. *International Journal of Remote Sensing*, *34*, 3084–3127.

Luo, C. -L., Chen, J., & Le, T. -C. (2008). Atmospheric correction on Landsat ETM + satellite image based on FLAASH model. *Protection Forest Science and Technology*, *5*, 46–48.

Matsunaga, T. (1994). A temperature–emissivity separation method using an empirical relationship between the mean, the maximum, and the minimum of the thermal infrared emissivity spectrum. *Journal of the Remote Sensing Society of Japan*, *14*, 28–39.

Meier, M. (1984). Contribution of small glaciers to global sea level. *Science*, *226*, 1418–1421.

Niclòs, R., Galve, J. M., Valiente, J. A., Estrela, M. J., & Coll, C. (2011). Accuracy assessment of land surface temperature retrievals from MSG2–SEVIRI data. *Remote Sensing of Environment*, *115*, 2126–2140.

Owen, L. A., Thackray, G., Anderson, R. S., Briner, J., Kaufman, D., Roe, G., et al. (2009). Integrated research on mountain glaciers: current status, priorities and future prospects. *Geomorphology*, *103*, 158–171.

Pope, A., & Rees, G. (2014). Using in situ spectra to explore Landsat classification of glacier surfaces. *International Journal of Applied Earth Observation and Geoinformation*, *27*, 42–52.

Price, J. C. (1984). Land surface temperature measurements from the split window channels of the NOAA 7 advanced very high resolution radiometer. *Journal of Geophysical Research — Atmospheres (1984–2012)*, *89*, 7231–7237.

Proy, C., Tanre, D., & Deschamps, P. (1989). Evaluation of topographic effects in remotely sensed data. *Remote Sensing of Environment*, *30*, 21–32.

Qin, Z. H., Karnieli, A., & Berliner, P. (2001). A mono-window algorithm for retrieving land surface temperature from Landsat TM data and its application to the Israel–Egypt border region. *International Journal of Remote Sensing*, *22*, 3719–3746.

Rees, W., & James, S. (1992). Angular variation of the infrared emissivity of ice and water surfaces. *International Journal of Remote Sensing*, *13*, 2873–2886.

Riggs, G. A., Hall, D. K., & Salomonson, V. V. (1994). A snow index for the Landsat thematic mapper and moderate resolution imaging spectroradiometer. *Geoscience and Remote Sensing Symposium, 1994. IGARSS'94. Surface and Atmospheric Remote Sensing: Technologies, Data Analysis and Interpretation., International* (pp. 1942–1944). IEEE.

Salisbury, J. W., D'Aria, D. M., & Wald, A. (1994). Measurements of thermal infrared spectral reflectance of frost, snow, and ice. *Journal of Geophysical Research — Solid Earth (1978–2012)*, *99*, 24235–24240.

Schott, J. R., Hook, S. J., Barsi, J. A., Markham, B. L., Miller, J., Padula, F. P., & Raqueno, N. G. (2012). Thermal infrared radiometric calibration of the entire Landsat 4, 5, and 7 archive (1982-2010). *Remote Sensing of Environment*, *122*, 41–49.

Simon, R., Tormos, T., & Danis, P. -A. (2014). Retrieving water surface temperature from archive LANDSAT thermal infrared data: Application of the mono-channel atmospheric correction algorithm over two freshwater reservoirs. *International Journal of Applied Earth Observation and Geoinformation*, *30*, 247–250.

Sobrino, J., El Kharraz, J., & Li, Z. -L. (2003). Surface temperature and water vapour retrieval from MODIS data. *International Journal of Remote Sensing*, *24*, 5161–5182.

Sobrino, J. A., Jiménez-Muñoz, J. C., & Paolini, L. (2004). Land surface temperature retrieval from LANDSAT TM 5. *Remote Sensing of Environment*, *90*, 434–440.

Sobrino, J., & Romaguera, M. (2004). Land surface temperature retrieval from MSG1–SEVIRI data. *Remote Sensing of Environment*, *92*, 247–254.

Strasser, U., Corripio, J., Pellicciotti, F., Burlando, P., Brock, B., & Funk, M. (2004). Spatial and temporal variability of meteorological variables at Haut Glacier d'Arolla (Switzerland) during the ablation season 2001: Measurements and simulations. *Journal of Geophysical Research — Atmospheres (1984–2012)*, *109*.

Tonooka, H. (2001). An atmospheric correction algorithm for thermal infrared multispectral data over land-a water-vapor scaling method. *IEEE Transactions on Geoscience and Remote Sensing*, *39*, 682–692.

Wald, A. E. (1994). Modeling thermal infrared (2–14 μm) reflectance spectra of frost and snow. *Journal of Geophysical Research — Solid Earth (1978–2012)*, *99*, 24241–24250.

Wan, Z. (2008). New refinements and validation of the MODIS land-surface temperature/emissivity products. *Remote Sensing of Environment*, *112*, 59–74.

Wan, Z., & Dozier, J. (1996). A generalized split-window algorithm for retrieving land-surface temperature from space. *IEEE Transactions on Geoscience and Remote Sensing*, *34*, 892–905.

Wan, Z., & Li, Z. L. (1997). A physics-based algorithm for retrieving land-surface emissivity and temperature from EOS/MODIS data. *IEEE Transactions on Geoscience and Remote Sensing*, *35*, 980–996.

Wan, Z., Zhang, Y., Zhang, Q., & Li, Z. L. (2002). Validation of the land-surface temperature products retrieved from terra moderate resolution imaging spectroradiometer data. *Remote Sensing of Environment*, *83*, 163–180.

Wang, N. L., He, J. Q., Pu, J. C., Jiang, X., & Jing, Z. F. (2010). Variations in equilibrium line altitude of the Qiyi Glacier, Qilian Mountains, over the past 50 years. *Chinese Science Bulletin*, *3814*–*3821*.

Wang, X., & Key, J. R. (2003). Recent trends in Arctic surface, cloud, and radiation properties from space. *Science*, *299*, 1725–1728.

Wang, Y., Wang, M., & Zhao, J. (2013). A comparison of MODIS LST retrievals with in situ observations from AWS over the Lambert Glacier Basin, East Antarctica. *International Journal of Geosciences*, *4*, 611–617.

Weng, Q., Lu, D., & Schubring, J. (2004). Estimation of land surface temperature–vegetation abundance relationship for urban heat island studies. *Remote Sensing of Environment*, *89*, 467–483.

Willis, I. C., Arnold, N. S., & Brock, B. W. (2002). Effect of snowpack removal on energy balance, melt and runoff in a small supraglacial catchment. *Hydrological Processes*, *16*, 2721–2749.

Yong, Z., Shiyin, L., & Yongjian, D. (2007). Glacier meltwater and runoff modelling, Keqicar Baqi glacier, southwestern Tien Shan, China. *Journal of Glaciology*, *53*, 91–98.

Zarco-Tejada, P. J., Rueda, C., & Ustin, S. (2003). Water content estimation in vegetation with MODIS reflectance data and model inversion methods. *Remote Sensing of Environment*, *85*, 109–124.

Zhang, G., Kang, S., Fujita, K., Huintjes, E., Xu, J., Yamazaki, T., et al. (2013). Energy and mass balance of Zhadang glacier surface, central Tibetan Plateau. *Journal of Glaciology*, *59*, 137–148.

Zhang, R., Tian, J., Su, H., Sun, X., Chen, S., & Xia, J. (2008). Two improvements of an operational two-layer model for terrestrial surface heat flux retrieval. *Sensors*, *8*, 6165–6187.